International Journal of Heat and Mass Transfer 140 (2019) 518–532

Contents lists available at ScienceDirect

International Journal of Heat and Mass Transfer

journal homepage: www.elsevier.com/locate/ijhmt

Thermal transport due to liquid jet impingement on superhydrophobic surfaces with isotropic slip: Isoflux wall

Matthew Searle *, Julie Crockett, Daniel Maynes

Department of Mechanical Engineering, Brigham Young University, 435 Crabtree Building, Provo, UT 84602, USA

ARTICLE INFO

Article history:
Received 17 July 2018
Received in revised form 27 March 2019
Accepted 30 May 2019

Keywords:
Superhydrophobic surface
Jet impingement
Convective heat transfer
Slip length
Temperature jump length
Isoflux wall

ABSTRACT

Thermal transport due to a liquid water jet impinging an isoflux superhydrophobic surface with isotropic slip was modeled analytically. An integral analysis of the transport equations resulting in a system of ordinary differential equations was solved numerically. Impingement on superhydrophobic surfaces greatly reduces the heat transfer that occurs relative to a smooth surface due to gas trapped in cavities on the surface. This results in an apparent slip velocity and temperature jump at the surface. Local and average Nusselt numbers are presented as a function of radial position (0 to 45 jet radii), jet Reynolds number (3×10^3 to 1.5×10^4), liquid Prandtl number (2 to 11), normalized slip length (0 to 0.2), and normalized temperature jump length (0 to 0.2). All results are compared to classical (no-slip, no temperature jump) behavior on a smooth surface. Although local Nusselt numbers for the isoflux scenario are greater than the corresponding isothermal case, the difference in Nusselt number between these two heating conditions becomes negligible as the temperature jump length increases to quantities realizable on superhydrophobic surfaces. These results may be utilized to explore heat transfer degradation in applications where smooth surfaces are replaced by superhydrophobic surfaces to avoid fouling.

1. Introduction

A common scenario for cooling in single phase heat transfer applications is liquid jet impingement on a heated surface. This yields some of the highest heat transfer coefficients encountered in single phase convection applications [1]. The schematic illustration in Fig. 1 shows a radial cross section of a liquid jet with velocity V, temperature T_j, and radius a impinging on a horizontal surface. A coordinate system is fixed at the impingement point with radial coordinate, r, and axial coordinate z, which increases moving upward from the impinged surface. The film thickness, h, the hydrodynamic boundary layer thickness, δ, and the thermal boundary layer thickness, δ_T, are shown developing outward from the stagnation point. In general, the wall may have an arbitrary wall heating condition. The present analysis considers the case of a uniform wall heat flux, q''_w, which is relevant for cooling applications such as thermal management of electronics and materials processing.

Prior investigators have considered liquid jet impingement on an isoflux surface for a classical surface [2–5,1]. These studies have considered heat transfer both in the stagnation and radial flow regions. An axisymmetric integral analysis of the mass, momentum, and energy equations with assumed polynomial velocity and temperature profiles allows solution of the boundary layer thicknesses and local Nusselt number [2,3,5]. Excellent agreement with experimental results was demonstrated [2,3]. These studies find that the heat transfer of the impinging liquid jet is determined by the jet Reynolds number, $Re = Q/\nu a$, and the Prandtl number, $Pr = \nu/\alpha$. Q is the jet flow rate, a is the jet radius, ν is the kinematic viscosity, and α is the thermal diffusivity. For $Pr > 1$ (the case of interest here), $\delta > \delta_T$, and the following flow regions (indicated in Fig. 1 panels (a) and (b)) are encountered as the jet spreads: (I) the stagnation region where the flow turns and δ and δ_T are constant with respect to position, (II) a region where δ and δ_T grow, (III) a region where δ_T grows and δ equals h, and, if $1 \leq Pr \leq 5$, (IV) a region where δ and δ_T equal h (panel (a)). As shown by Liu and Lienhard, if $Pr > 5$, the thermal boundary layer no longer grows to the size of the film and this is denoted in panel (b) [2].

Impinging jets on superhydrophobic (SH) surfaces yield altered hydrodynamics and thermal transport [6–9]. It is of interest to study thermal transport on these surfaces to determine how it is influenced when SH surfaces are utilized for their desirable properties of drag reduction [10–13] and self-cleaning [14–17]. SH surfaces are created by combining micro/nano-roughness with

* Corresponding author.
E-mail address: matthew.c.searle@gmail.com (M. Searle).

https://doi.org/10.1016/j.ijheatmasstransfer.2019.05.113
0017-9310/

Nomenclature

a	jet radius
c	liquid specific heat
h	liquid film height
$\hat{h}$	normalized film height $\hat{h} = h/a$
$\hat{h}_0$	normalized liquid film height at the end of region II
$\hat{h}_1$	normalized film height at the end of region III
H	control volume height
k	liquid thermal conductivity
$\dot{m}$	mass flow rate leaving the top control volume surface
Nu	Nusselt number $Nu = q''_w a\pi/(k(T_w - T_j))$
Nu_T	isothermal Nusselt number
Nu_F	isoflux Nusselt number
$\overline{Nu}$	radially-averaged Nusselt number
$\overline{Nu}_0$	average Nusselt number for no-slip and no temperature jump case
Pr	Prandtl number $Pr = \nu/\alpha$
Q	jet volumetric flow rate
q''_w	wall heat flux
r	radial coordinate
$\hat{r}$	normalized radial coordinate $\hat{r} = r/a$
$\hat{r}_s$	normalized radial coordinate at end of region I
$\hat{r}_0$	normalized radial coordinate at end of region II
$\hat{r}_1$	normalized radial coordinate at end of region III
Re	Reynolds number $Re = Q/(a\nu)$
T	local liquid temperature
T_{fs}	free surface temperature
T_j	initial jet temperature
T_w	wall temperature
u	radial velocity
$\hat{u}$	normalized velocity $\hat{u} = u/V$
U_{fs}	free surface velocity
$\hat{U}_{fs}$	normalized free surface velocity $\hat{U}_{fs} = U_{fs}/V$
V	jet velocity
z	axial coordinate
$\hat{z}$	normalized axial coordinate $\hat{z} = z/a$

Greek Symbols

α	thermal diffusivity
δ	hydrodynamic boundary layer thickness
$\hat{\delta}$	normalized hydrodynamic boundary layer thickness $\hat{\delta} = \delta/a$
$\hat{\delta}_s$	normalized hydrodynamic boundary layer thickness in region I
δ_T	thermal boundary layer thickness
$\hat{\delta}_T$	normalized thermal boundary layer thickness $\hat{\delta}_T = \delta_T/a$
$\hat{\delta}_{Ts}$	normalized thermal boundary layer thickness in region I
$\hat{\delta}_{T0}$	normalized thermal boundary layer thickness at the end of region II
Δr	control volume radial thickness
ΔT	temperature jump $\Delta T = T_w - T(r, z = 0)$
θ	non-dimensional temperature $\theta = k(T - T_j)/(q''_w a)$
θ_{fs}	non-dimensional free surface temperature $\theta_{fs} = k(T_{fs} - T_j)/(q''_w a)$
λ	hydrodynamic slip length
$\hat{\lambda}$	normalized hydrodynamic slip length $\hat{\lambda} = \lambda/a$
λ_T	temperature jump length
$\hat{\lambda}_T$	normalized temperature jump length $\hat{\lambda}_T = \lambda_T/a$
ν	kinematic viscosity
ρ	fluid density

hydrophobic chemistry. This combination leads to static solid-liquid contact angles greater than 150° [18].

Superhydrophobic surfaces are of interest to the heat transfer community because they have anti-fouling properties. Fouling of heat transfer surfaces can add resistance, which dramatically decreases thermal transport. It is important to model how these surfaces inhibit heat transfer so that cost-benefit analyses of exchanging superhydrophobic surfaces for conventional surfaces may be performed. The decrease in heat transfer at a clean SH surface impinged by a liquid jet may be less than the decrease in heat transfer at a fouled, conventional surface experiencing the same flow.

Drag reduction and self-cleaning behavior are the result of the composite boundary condition present on these surfaces. Due to surface roughness and material hydrophobicity, liquid water is prevented from penetrating the cavities between microfeatures when the liquid pressure is sufficiently small. Instead, the cavities remain filled with air and/or water vapor and a meniscus spans each cavity.

The relevant boundary conditions for modeling fluid flow over these surfaces are a no-slip condition at the top of each microfeature and a free shear condition at each gas-liquid meniscus. An aggregate, single macroscale boundary condition can instead be introduced at the wall as an apparent slip velocity (u_s), which is proportional to the wall shear (τ_w), such that $u_s = \tau_w \lambda/\mu$[13,19]. Here μ is the dynamic viscosity and λ is the slip length, which may be physically interpreted as the distance into the wall that the apparent velocity profile must be extrapolated to reach the no-slip condition. A slip velocity at the wall leads to a decrease in wall shear stress and an overall drag reduction. Another effect of the menisci over the cavities is a decrease in aggregate surface energy for liquid water droplets, resulting in increased contact angle and droplet rolling behavior. This dynamic allows easy removal of contaminants from SH surfaces by rolling droplets [17].

A discussion of slip hydrodynamics is incomplete without reference to molecular slip in the field of high Knudsen number gas flow. Although the physical mechanism of slip is different (rarefied gas flow vs. apparent slip due to alternating no-slip wall and shear-free meniscus), the Navier slip hypothesis may be applied to both. Relevant to the developing flow in the present jet impingement model are prior works presenting analytical models for slip flow in the hydrodynamic entrance region of microchannels [20,21].

For completeness, we also reference research which has addressed maintaining non-wetted cavities, an essential condition for the results of this paper, through a variety of techniques including surface heating and re-entrant cavities [22,23].

Thermal boundary conditions on SH surfaces are also altered. Metallic microfeatures have thermal conductivities three orders of magnitude higher than that of the air/water vapor mixture which fills the cavities. Thus, it is appropriate to model the gas-liquid interface as adiabatic and match the temperature at the solid-liquid interface. Numerical studies have demonstrated the validity of this approximation [24]. Again, these alternating boundary conditions may be modeled with an aggregate boundary condition, where the apparent wall temperature jump may be expressed as $\Delta T_w = q''_w \lambda_T/k$, where q''_w is the wall heat flux [25–27]. Here, k is the thermal conductivity of the liquid and the temperature jump length, λ_T, is the thermal analog of λ.

The first region shown in Fig. 1 is the stagnation region, where the liquid impinges normally on the substrate and the flow accelerates in the radial direction. In a classical stagnation flow, a uniform flow normal to the surface impinges a substrate and this

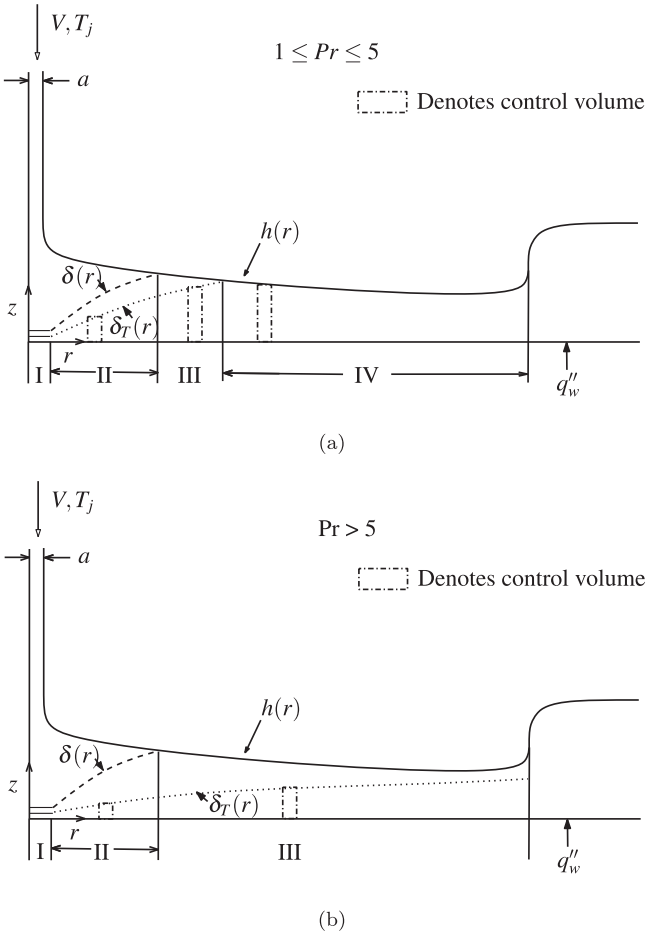

Fig. 1. An impinging liquid jet is illustrated schematically with a radial cross section spanning from the jet centerline (left) to beyond the hydraulic jump (right). The jet initially has a uniform velocity, V, and temperature, T_j. The liquid impinges on a horizontal surface which is heated with an isoflux boundary condition maintaining a uniform heat flux, q''_w. The hydrodynamic boundary layer thickness, δ, thermal boundary layer thickness, δ_T, and film height, h, are shown. The flow of the spreading jet is subdivided into four regions, numbered I–IV. All four regions are present in panel (a) ($1 \leqslant Pr \leqslant 5$). In panel (b) $Pr > 5$ and region IV is absent since δ_T is always smaller than h.

provides a good estimate of the dynamics near the impingement point in liquid jets. The SH boundary conditions of slip and temperature jump have previously been considered for classical stagnation flow from an analytical perspective. Here similarity solutions have been obtained for axisymmetric and planar flows stagnating on a surface with isotropic and anisotropic slip length and both stationary and moving plates have been considered [28–30]. Heat transfer from isothermal surfaces has been modeled under conditions of isotropic slip and temperature jump [29] and these prior solutions are utilized in the present work to approximate the heat transfer within the stagnation region of the impinging jet (Section 2.3). These prior results indicate heat transfer increases with increasing slip length and decreases with increasing temperature jump length.

Within the radial flow region, the hydrodynamics of jet impingement on a SH surface with isotropic and anisotropic slip have been modeled analytically [6–8]. Common microstructures of SH surfaces are posts and ribs. The conditions of isotropic slip may be achieved with post micropatterning and anisotropic slip with rib micropatterning. For both of these scenarios, the slip length was held constant moving radially away from the impingement point. These studies found that increasing the hydrodynamic slip length yields a similar effect as increasing the jet Reynolds number. Specifically, the thickness of the spreading film decreased and the location of a hydraulic jump (or film breakup with droplets) moved outward as the slip length increased. Model predictions for the location of the hydraulic jump and/or breakup agreed well with companion experiments, suggesting that assuming constant slip length in the flow direction (radial) provides a good model for this scenario.

Only a single study has explored the scenario of a jet impinging on a heated SH surface. Specifically, the constant wall temperature condition surface with isotropic slip was considered [9]. This study showed that the Nusselt number drops dramatically as the slip length and temperature jump length increased. Additionally, the dependence of thermal transport on flow conditions (Reynolds number and Prandtl number) vanished as temperature jump length increased and variations in the temperature jump length yield much stronger influence on the transport than equivalent changes in the hydrodynamic slip length.

In the present study, we consider a jet impinging at a SH surface with isotropic slip length and temperature jump length where a uniform heat flux is applied to the surface (isoflux condition). Both the stagnation and radial flow regions are considered, with the stagnation region modeled by a prior solution [29] and the radial flow region modeled by an integral analysis defined here. This scenario has not been previously considered and is valuable, as mentioned earlier, for cooling applications such as thermal management of electronics and materials processing. In the following sections, the analytical methodology is presented and the results are benchmarked with prior work. Local and average Nusselt numbers are presented for varying radial coordinate, Reynolds number, Prandtl number, slip length, and temperature jump length. These results are discussed and conclusions from the work are summarized.

2. Analysis

2.1. Model description

The scenario of a cool liquid jet impinging on a SHPo surface may be modeled by performing an integral analysis of each of the four regions described earlier and applying slip and temperature jump boundary conditions at the wall. The hydrodynamic solution now depends on λ as well as Re and the thermal transport solution depends on λ_T and Pr.

The surface type considered in this study is one with constant isotropic slip length and temperature jump length and is characteristic of post patterned micro-features. It has been shown by several investigators that in laminar internal flow the slip length is a constant value (independent of flow direction) [31,32]. This is true regardless of Reynolds number. Similar analysis has been performed for thermal transport [33,34] with a similar conclusion regarding temperature jump length. While the present work is a boundary layer flow as opposed to a fully-developed internal flow, the analysis is constrained to a laminar flow. In a boundary layer flow, the wall shear stress generally decreases along the streamwise direction, which is analogous to an internal flow with a varying Reynolds number. Thus if the slip length is independent of Reynolds number in a fully-developed internal flow, this should also be the case in a boundary layer flow.

Additionally, the assumption of constant slip length (independent of Reynolds number) is necessary for analytical tractability. The full jet impingement problem could not be resolved numerically, unlike fully-developed channel flow, since all post-cavity modules would need to be modeled as opposed to a single post-cavity module with periodic boundary conditions [33,34].

In this analysis, the surface tension is assumed to be constant. Marangoni convection was shown previously to be negligible for high-speed shear flows at superhydrophobic surfaces [24]. Further, the meniscus spanning the microcavities is approximated as being a planar, shear-free region. Physically, the meniscus will have curvature and the curvature will likely vary with radial location due to flow inertia. However, the influence of meniscus curvature on the hydrodynamics of flow over superhydrophobic surfaces has been considered previously by several investigators and it has been demonstrated that for a first-order model it is reasonable to approximate the meniscus as a planar, shear-free region [19,26,32].

The values of constant λ and λ_T are determined by analysis of the diffusion-dominated flow near the wall. The present analysis intends that microscale analyses be applied to determine λ and λ_T for a certain microstructure. The appropriate macroscale solution of the impinging jet is presently obtained for a range of λ and λ_T. Calculation of λ is well-defined [19,13]. More recent studies have performed diffusion-dominated thermal analyses to determine λ_T for a variety of microfeature geometries [25–27,35]. These have been accompanied by computational simulations where λ_T has been calculated from the flow field [33,34]. These studies indicate that the ratio of λ_T to λ is on the order of 1. In the subsequent analysis, we assume that the ratio is 1 or, equivalently, $\lambda = \lambda_T$. The equations developed here may easily be implemented to solve for any ratio λ_T/λ as illustrated in Section 3.4.

All regions were solved for varying Re (3×10^3 to 1.5×10^4), Pr (2 to 11), $\hat{\lambda}$ (0 to 0.2), and $\hat{\lambda}_T$ (0 to 0.2) for $\hat{r}$ varying from 0 to 45 where the hat indicates normalization with respect to a. All lengths in this study are normalized in this manner. The differential equation solver utilized was an explicit eighth-order Runge-Kutta method as implemented in the numerical solver software Mathematica®. The resulting numerical error in determining the local Nusselt number is at most $\pm 1 \times 10^{-4}$.

2.2. Fundamental equations

Integral forms of conservation (mass and energy) are applied to annular control volumes of radius r, thickness Δr, and height H (see Fig. 1) yielding

$$\dot{m} = -2\pi\rho \frac{\partial}{\partial r}\left(r \int_0^H u(r,z)\,dz\right)\Delta r \tag{1}$$

and

$$-\dot{m}cT(r,H) + q''_w(2\pi r)\Delta r - 2\pi\rho c \frac{\partial}{\partial r}\left(r \int_0^H u(r,z)T(r,z)\,dz\right)\Delta r = 0 \tag{2}$$

where $\dot{m}$ is the mass flow rate through the top surface of the control volume, u is the local liquid radial velocity, T is the local liquid temperature, ρ is the liquid density, and c is the liquid specific heat. The hydrodynamic solution for this scenario was obtained previously and results for the velocity field are included as needed [6].

2.3. Region I: Stagnation region

The stagnation region is modeled using a similarity solution obtained previously for axisymmetric stagnation flow on a non-moving surface with isotropic slip velocity and temperature jump [29]. The solution satisfies the differential boundary layer equations for mass, momentum (axial and radial directions), and energy. At the wall, the slip velocity and temperature jump boundary conditions are applied. The slip length and temperature jump length parameters in the solution (λ_W and β) are related to the slip length and temperature jump length utilized in the present work (λ and λ_T) by

$$\lambda_W = \sqrt{CRe/\pi}\lambda \tag{3}$$

$$\beta = \sqrt{CRe/\pi}\lambda_T \tag{4}$$

The stagnation Nusselt number as defined in the present paper may be obtained from the prior results [29] as

$$Nu = -\sqrt{\pi\ C\ Re}\ \left.\frac{\partial\theta_s}{\partial\eta}\right|_{\eta=0} \tag{5}$$

C is a dimensionless constant which is related to the radial velocity gradient and was obtained previously to be 0.458 for an impinging jet [4]. θ_s and η are similarity variables from the prior results which indicate respectively, the temperature profile and the wall normal coordinate. Definitions for $\theta_s, \eta, \lambda_W$, and β and details concerning the solution may be obtained from the prior work [29]. To avoid confusion with the temperature profile, θ, defined with this work, these similarity variables are not listed in the nomenclature.

Although the above similarity solution was obtained for an isothermal surface, within the stagnation region, isoflux and isothermal Nusselt numbers will be the same since the boundary layer thicknesses are uniform [1].

δ_s and δ_{Ts}, the constant hydrodynamic and thermal boundary layer thicknesses, are used as the initial conditions at the end of the stagnation region, $\hat{r}_s = 0.9$, for the subsequent region. These boundary layer thicknesses are calculated from the similarity solution in the classical manner by numerically solving for the location at which the velocity and temperature profiles have reached 99% of their respective freestream values, $\eta = \eta_{99\%}$ and $\eta_T = \eta_{T99\%}$, respectively, with the equations being solved expressed as

$$\left.\frac{\partial f}{\partial\eta}\right|_{\eta=\eta_{99\%}} = 0.99 \tag{6}$$

and

$$\theta(\eta_{T99\%}) = 0.01 \tag{7}$$

$\eta_{99\%}$ and $\eta_T = \eta_{T99\%}$ are then substituted into

$$\hat{\delta}_s = \eta_{99\%}\sqrt{\frac{\pi}{CRe}} \tag{8}$$

$$\hat{\delta}_{Ts} = \eta_{T99\%}\sqrt{\frac{\pi}{CRe}} \tag{9}$$

yielding $\hat{\delta}_s$ and $\hat{\delta}_{Ts}$.

The end of the stagnation region is defined following the prior work of Liu et al. [4], in which an analytical model including surface tension for the inviscid region of the impinging jet was presented. The model found that true stagnation flow (characterized by a linear rise in the free stream velocity) extended to $\hat{r} = 0.7$ and that modeling the flow in this manner was a reasonable approximation to $\hat{r} = 1.5$. The value of $\hat{r} = 0.9$ was selected because it was within this range, near $\hat{r} = 0.7$, and minimized the discontinuity between results for the stagnation flow and radial flow models.

2.4. Region II: Developing boundary layers

Upon leaving the stagnation region, the flow is primarily in the radial direction and $\hat{\delta}$ and $\hat{\delta}_T$ increase as the radial coordinate increases. Since $Pr > 1, \delta$ grows more quickly than δ_T. We note that a free surface is now present and creates a shear free boundary condition at the height of the liquid film, h. Since this replaces

the condition of uniform, wall-directed flow in region I, that region's similarity solution is no longer valid in region II and beyond. Region II concludes when δ merges with h. The height of the control volume in Region II is set to $H = \delta_T$ where the local temperature is equal to the jet temperature, $T(r, z = \delta_T) = T_j$. This control volume is displayed in panels (a) and (b) of Fig. 1. Substituting Eq. (1) into Eq. (2) yields the following equation for region II

$$q''_w = \frac{\rho c}{r}\frac{\partial}{\partial r}\left(r\int_0^{\delta_T} u(T(r,z) - T_j)\,dz\right) \tag{10}$$

The velocity profile was previously obtained for this region to be

$$u = \frac{V}{\frac{2}{3}\delta + \lambda}\left[\lambda + z - \frac{z^3}{3\delta^2}\right] \tag{11}$$

A cubic temperature profile is assumed

$$T = a + bz + cz^2 + dz^3 \tag{12}$$

To which the following boundary conditions are applied

$$-k\left.\frac{\partial T}{\partial z}\right|_{z=0} = q''_w \tag{13}$$

$$T(r, z = \delta_T) = T_j \tag{14}$$

$$\left.\frac{\partial T}{\partial z}\right|_{z=\delta_T} = 0 \tag{15}$$

$$\left.\frac{\partial^2 T}{\partial z^2}\right|_{z=0} = 0 \tag{16}$$

The choice of a third-order polynomial is necessary since the hydrodynamic boundary layer is a third-order profile [6] and this allows δ to equal δ_T when $Pr = 1$. Applying these boundary conditions to Eq. (12) and solving for coefficients a–d yields

$$T - T_j = \frac{q''_w}{3k}\left(2\delta_T - 3z + \frac{z^3}{\delta_T^2}\right) \tag{17}$$

The assumed velocity (Eq. (11)) and temperature (Eq. (17)) profiles are substituted into Eq. (10). The resulting relationship is

$$\frac{\pi\hat{r}}{RePr} = \frac{\partial}{\partial\hat{r}}\frac{\hat{r}\hat{\delta}_T^2\left(2\hat{\delta}_T^3 + 7\hat{\delta}^2\right)\left(4\hat{\delta}_T + 15\hat{\lambda}\right)}{140\hat{\delta}^2\left(2\hat{\delta} + 3\hat{\lambda}\right)} \tag{18}$$

Prior hydrodynamic solutions to the integral mass and momentum equations gives the following equations [6]

$$\hat{h} = \frac{1}{2\hat{r}} + \frac{\hat{\delta}^2}{4\left(\frac{2}{3}\hat{\delta} + \hat{\lambda}\right)} \tag{19}$$

and

$$\frac{\pi\hat{r}}{Re} = \left(\frac{2}{3}\hat{\delta} + \hat{\lambda}\right)\frac{d}{d\hat{r}}\left[\hat{r}\hat{\delta}^2\left(\frac{13}{210}\hat{\delta} + \frac{1}{4}\hat{\lambda}\right)\left(\frac{2}{3}\hat{\delta} + \hat{\lambda}\right)^{-2}\right] \tag{20}$$

$\hat{\delta}$ and $\hat{\delta}_T$ are obtained as functions of $\hat{r}$ by numerically solving the system of differential equations defined by Eqs. (18) and (20) subject to the initial conditions $\hat{\delta}(\hat{r} = \hat{r}_s) = \hat{\delta}_s$ and $\hat{\delta}_T(\hat{r} = \hat{r}_s) = \hat{\delta}_{Ts}$. $\hat{h}$ is found by substituting the results for $\hat{\delta}$ into Eq. (19). The endpoint of region II is found by numerically finding $\hat{r}$ where $\hat{\delta}$ equals $\hat{h}$. This radius is labeled $\hat{r}_0$ and the values of $\hat{\delta}_T$ and $\hat{h}$ at this point are labeled $\hat{\delta}_{T0}$ and $\hat{h}_0$, respectively.

We seek to obtain the local Nusselt number, Nu, which is defined in the normal manner as

$$Nu = q''_w a\pi/\left(k(T_w(r) - T_j)\right) \tag{21}$$

Recalling that there is a temperature jump at the wall, we can obtain a relationship which is valid in any region between the wall temperature, $T_w(r)$, and the temperature given by a profile at $T(r, z = 0)$, the difference of which is the temperature jump, $\Delta T_w = T_w - T(r, z = 0)$. The temperature jump is proportional to the heat flux, $\Delta T_w = (q''_w\lambda_T)/k$[26]. Combining these two results yields

$$T_w(r) = q''_w\lambda_T/k + T(r, z = 0) \tag{22}$$

which is valid in all regions. Nu may be obtained for region II by substituting for $T_w(r) - T_j$ in Eq. (21). Eq. (17) is evaluated at the wall yielding

$$T(r, z = 0) - T_j = \frac{2q''_w\delta_T}{3k} \tag{23}$$

T_j is subtracted from both sides of Eqs. (22) and (23) is substituted yielding

$$T_w(r) - T_j = \frac{q''_w\lambda_T}{k} + \frac{2q''_w\delta_T}{3k} \tag{24}$$

Finally, this result is substituted into Eq. (21) resulting in Nu as a function of $\hat{\delta}_T$

$$Nu = \frac{\pi}{\hat{\lambda}_T + \frac{2}{3}\hat{\delta}_T} \tag{25}$$

2.5. Region III: Further developing thermal boundary layer

After region II, δ_T continues to grow until it to merges with h. The energy equation (Eq. (10)) and temperature profiles (Eq. (17)) remain the same as those in region II but will be applied to the control volume shown in region III of Fig. 1 panels (a) and (b). The velocity profile must be modified since the top boundary is a shear free condition instead of matched velocity. The velocity at the top surface, U_{fs}, becomes a function of r such that the velocity profile is

$$\hat{u} = \frac{\widehat{U}_{fs}}{\frac{2}{3}\hat{h} + \hat{\lambda}}\left[\hat{\lambda} + \hat{z} - \frac{\hat{z}^3}{3\hat{h}^2}\right] \tag{26}$$

where the hats on u and U_{fs} indicate normalization by V and all velocities are normalized in this manner. $\widehat{U}_{fs}$ was obtained previously [6] by applying conservation of mass (Eq. (1)) as

$$\widehat{U}_{fs} = \frac{\frac{2}{3}\hat{h} + \hat{\lambda}}{2\hat{h}\hat{r}\left(\frac{5}{12}\hat{h} + \hat{\lambda}\right)} \tag{27}$$

Eqs. (27), (26) and (17) are substituted into the energy equation (Eq. (10)) yielding

$$\frac{\pi\hat{r}}{RePr} = \frac{\partial}{\partial\hat{r}}\frac{\hat{\delta}_T^2\left(2\hat{\delta}_T^3 + 7\hat{h}^2\left(4\hat{\delta}_T + 15\hat{\lambda}\right)\right)}{70\hat{h}^3\left(5\hat{h} + 12\hat{\lambda}\right)} \tag{28}$$

The momentum equation for this region was obtained previously [6] as

$$-\frac{2\pi}{Re} = \hat{h}\left(\frac{5}{12}\hat{h} + \hat{\lambda}\right)\frac{d}{d\hat{r}}\left[\hat{r}^{-1}\hat{h}^{-1}\left(\frac{68}{315}\hat{h}^2 + \frac{5}{6}\hat{h}\hat{\lambda} + \hat{\lambda}^2\right)\left(\frac{5}{12}\hat{h} + \hat{\lambda}\right)^{-2}\right] \tag{29}$$

The system of differential equations defined by Eqs. (28) and (29) is solved numerically to obtain $\hat{h}$ and $\hat{\delta}_T$ as functions of $\hat{r}$ subject to the initial conditions $\hat{h}(\hat{r} = \hat{r}_0) = \hat{h}_0$ and $\hat{\delta}_T(\hat{r} = \hat{r}_0) = \hat{\delta}_{T0}$. $\hat{\delta}_T$

and $\hat{h}$ were solved through 45 jet radii (well beyond the intersection point between $\hat{\delta}_T$ and $\hat{h}$, if it occurs). *Nu* is determined by the same equation obtained for region II (Eq. (25)). As discussed earlier in Section 2.1, it is possible for $\hat{\delta}_T$ to not intersect $\hat{h}$. A numerical root finding routine was applied to determine if this intersection did occur. If so, the radius was labeled $\hat{r}_1$ and the value of $\hat{h}$ obtained at this point was labeled $\hat{h}_1$. These values were used as the initial conditions for the differential equations defined in region IV. Region IV was not solved if $\hat{\delta}_T$ did not reach $\hat{h}$.

2.6. Region IV: Both boundary layers merged

In region IV, δ_T has merged with h and the control volume height is set to $H = h$ with $\dot{m} = 0$. This control volume is shown in Fig. 1 panel (a) region IV. Substituting these results into the energy equation Eq. (2) yields

$$q''_w = \frac{\rho c}{r}\frac{\partial}{\partial r}\left(r\int_0^h uT\,dz\right) \tag{30}$$

The velocity profile remains the same as that derived in region III (Eq. (26)) but new boundary conditions must be applied to the temperature profile so that the top boundary condition is now adiabatic (assuming negligible evaporation) instead of a fixed temperature. Consequently, the free surface temperature, T_{fs}, varies with r. To satisfy these new conditions, the second and third boundary conditions defined for the temperature profile in region III (Eqs. (14) and (15)) are replaced with the following boundary conditions

$$T(r, z = h) = T_{fs}(r) \tag{31}$$

$$\left.\frac{\partial T}{\partial z}\right|_{z=h} = 0 \tag{32}$$

Applying these boundary conditions, the temperature profile for region IV is obtained as

$$T(r,z) = T_{fs} + \frac{q''_w}{3k}\left(2h - 3z + \frac{z^3}{h^2}\right) \tag{33}$$

Substituting $\hat{U}_{fs}$ (Eq. (27)) into the velocity profile (Eq. (26)) and this result and the temperature profile (Eq. (33)) into the energy equation (Eq. (30)) yields

$$\frac{\pi\hat{r}}{RePr} = \frac{\partial}{\partial\hat{r}}\left(\frac{\theta_{fs}}{2} + \frac{\hat{h}}{8} - \frac{71\hat{h}^2}{280\left(5\hat{h} + 12\hat{\lambda}\right)}\right) \tag{34}$$

where $\theta_{fs} = k(T_{fs} - T_j)/(q''_w a)$ is the normalized free surface temperature. The system of differential equations defined by Eqs. (29) and (34) is solved numerically for $\hat{h}$ and θ_{fs} as functions of $\hat{r}$ subject to the initial conditions $\hat{h}(\hat{r} = \hat{r}_1) = \hat{h}_1$ and $\theta_{fs}(\hat{r} = \hat{r}_1) = 0$.

Nu may be determined by substituting for $T_w(r) - T_j$ in Eq. (21). To find this, first Eq. (33) is evaluated at $\hat{z} = 0$ yielding

$$T(z = 0) = T_{fs} + \frac{2q''_w h}{3k} \tag{35}$$

Then Eq. (35) is substituted into Eq. (22) and T_j is subtracted from both sides

$$T_w(r) - T_j = \frac{q''_w \lambda_T}{k} + \frac{2q''_w h}{3k} + T_{fs} - T_j \tag{36}$$

Finally, Eq. (36) is substituted into Eq. (21) yielding

$$Nu = \frac{\pi}{\hat{\lambda}_T + \frac{2}{3}\hat{h} + \theta_{fs}} \tag{37}$$

3. Results

The results section proceeds as follows: results obtained here for the no-slip scenario are compared with prior results. Then, the influence of temperature jump length on the thermal boundary layer thickness, Nusselt number, and local temperature distributions are explored. It is shown that the Nusselt number results for both the isothermal and isoflux wall scenarios merge together as the temperature jump length increases. Finally, results are presented for the average Nusselt number.

3.1. Comparison with previous results

Local Nusselt number is shown as a function of $\hat{r}$ in Fig. 2 for the no-slip and no-temperature jump scenario at $Pr = 5$ and at $Re = 3 \times 10^3, 9 \times 10^3$, and 1.5×10^4. Excellent agreement is shown with prior analytical solutions obtained by Ma [5] and Liu [2]. Similarly good agreement was also demonstrated at $Pr = 2$ and $Pr = 11$, although these results are not shown here. The goodness

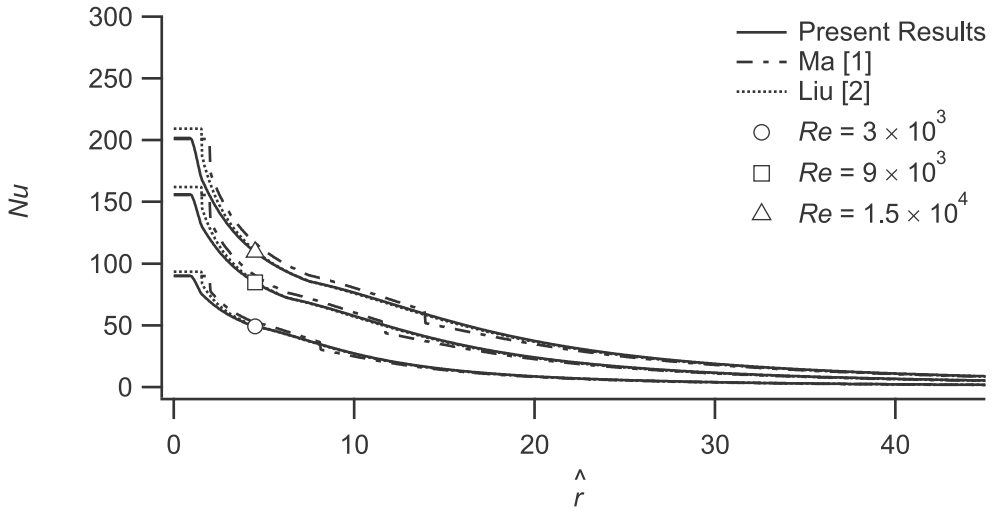

Fig. 2. The present solution for the local Nusselt number for the no-slip and no temperature jump scenario at $Pr = 5$ and Re varying from 3×10^3 to 1.5×10^4 is plotted as a function of $\hat{r}$. Previous solutions by Ma [1] and Liu [2] are included for comparison.

of the agreement with prior results for the no-slip case provide a benchmarking of our modeling approach.

3.2. Local behavior: Influence of slip velocity and temperature jump, Reynolds number, and Prandtl number

This section of the paper explores the influence of slip and temperature jump on local features in the thermal boundary layer. Shown in Fig. 3 are $\hat{h}$ and $\hat{\delta}_T$ as functions of $\hat{r}$. Results are shown in three panels, with $\hat{\lambda}_T, Re$, and Pr respectively varying in each panel, while the other parameters remain fixed. The transitions in the thermal boundary layer from region I to II, region II to III, and region III to IV are marked with an asterisk, plus sign, and diagonal cross mark, respectively. These transition locations correspond to radial locations r_s, r_0, and r_1. In panel (a), $\hat{\lambda}_T$ varies from 0 to 0.2 (Pr = 5, $Re = 9 \times 10^3$) and the results reveal that an increase in $\hat{\lambda}$ (accompanied by an equivalent increase in $\hat{\lambda}_T$) results in a notable decrease in $\hat{\delta}_T$.

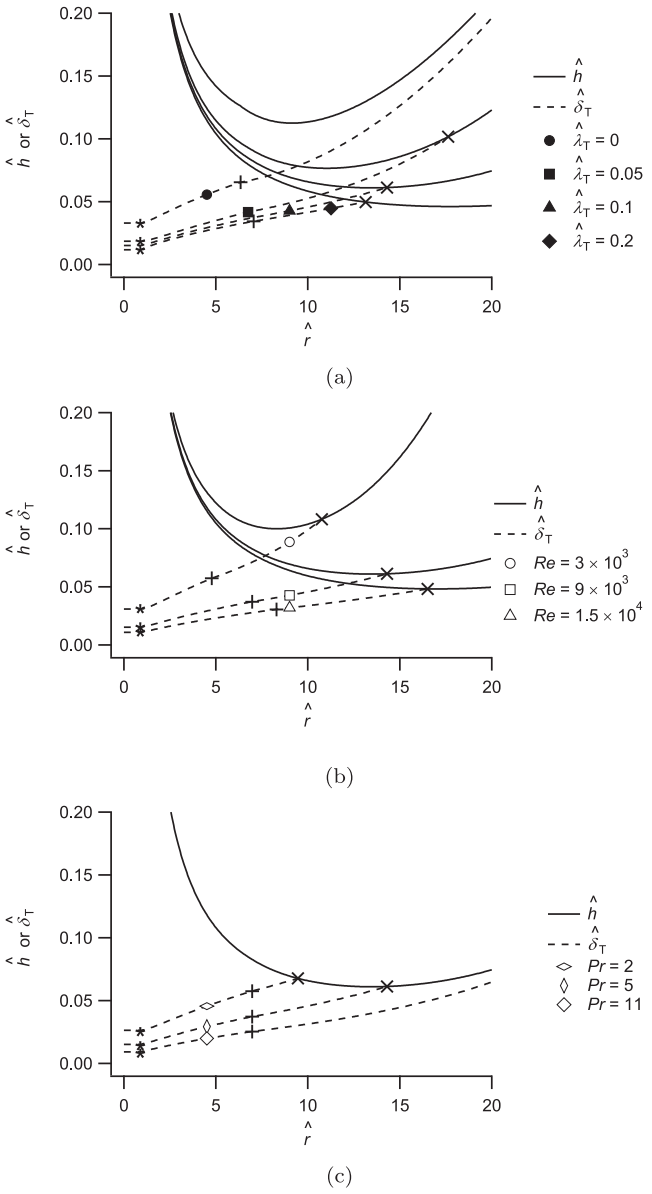

Fig. 3. The normalized local thermal boundary layer thickness and film height as functions of $\hat{r}$. In panel (a), Pr = 5 and $Re = 9 \times 10^3$, with $\hat{\lambda}_T$ increasing from 0 to 0.2. In panel (b), $Pr = 5$ and $\hat{\lambda}_T = 0.1$, with Re varying from 3×10^3 to 1.5×10^4. In panel (c), $Re = 9 \times 10^3$ and $\hat{\lambda}_T = 0.1$, with Pr varying from 2 to 11. The region I to II transition, region II to III transition, and region III to IV transition are marked with an asterisk, plus sign, and diagonal cross mark, respectively. Some transition marks are omitted for clarity in panel (a).

This decrease is expected from hydrodynamic considerations, since an increase in $\hat{\lambda}$ increases the momentum in the boundary layer and leads to a thinning of the layer to satisfy continuity. Note that $\hat{\delta}_T$ never merges with the height of the thin film, $\hat{h}$, for the $\hat{\lambda}_T = 0$ scenario, and thus region IV does not exist for this case. However, as $\hat{\lambda}_T$ increases, $\hat{\delta}_T$ merges with $\hat{h}$ at $\hat{r}_1$ (indicated by a diagonal cross mark) and region IV does exist. Increasing $\hat{\lambda}_T$ results in merging of the boundary layer thickness with the film height at smaller $\hat{r}_1$.

Shown in panel (b) of Fig. 3 are results with $Pr = 5$, $\hat{\lambda}_T = 0.1$, and Re varying from 3×10^3 to 1.5×10^4. The $\hat{\delta}_T$ variation with $\hat{r}$ for this $\hat{\lambda}_T$ exhibits classical behavior as Re is increased (decreasing $\hat{\delta}_T$ due to the decreasing hydrodynamic boundary layer thickness). $\hat{\lambda}_T = 0.1$ is sufficiently large that $\hat{\delta}_T$ merges with $\hat{h}$ for each Re shown. The influence of variation in Pr is demonstrated in panel (c), where $Re = 9 \times 10^4$, $\hat{\lambda}_T = 0.1$, and Pr varies from 2 to 11. The $Pr = 5$ case (indicated by an open, vertical diamond) is identical to the case shown with a solid triangle in panel (a). $\hat{\delta}_T$ decreases as Pr increases and $\hat{r}_1$ (indicated by a diagonal cross mark) increases as well. This occurs since the thermal diffusivity decreases relative to the kinematic viscosity as Pr increases. At $Pr = 11$, Pr has become sufficiently large such that $\hat{\delta}_T$ no longer merges with $\hat{h}$, even at large $\hat{r}$.

Next we explore the influence of superhydrophobicity ($\hat{\lambda}_T$) on the non-dimensional temperature profile, θ. $\theta = k(T - T_j)/(q''a)$ is shown as a function of the normalized vertical coordinate, $\hat{z}$, in Fig. 4 for several scenarios. In each panel of the figure, θ is plotted as a function of the $\hat{z}$-coordinate from $\hat{z} = 0$ to $\hat{z} = \hat{h}$ (the height of the film). In the left three panels (a, c, e), the radial coordinate is fixed at $\hat{r} = 10$ and, in the right three panels (b, d, f), $\hat{r} = 30$. The top panels (a,b) provide profiles at $Re = 9 \times 10^3$ and $Pr = 5$ with $\hat{\lambda}_T$ varying from 0 to 0.2. The second row of panels provides profiles at $Pr = 5$ and $\hat{\lambda}_T = 0.1$, and Re varying from 3×10^3 to 1.5×10^4. In the bottom row (e, f), $Re = 9 \times 10^3$ and $\hat{\lambda}_T = 0.1$ and Pr varies from 2 to 11.

As defined, θ approaches zero as the local temperature approaches the incoming jet temperature. For all θ profiles shown in Fig. 4 at $\hat{r} = 10$ (panels a, c, and e), the radial location corresponds to region III of the thin film. Recall that in region III, the hydrodynamic boundary layer has merged with the height of the thin film, while the thermal boundary layer has not. Thus, the profiles shown all level off at zero at sufficiently large $\hat{z}$, with the wall-normal location where this occurs being the thermal boundary layer thickness. θ thus remains zero through the rest of the thin film up to $\hat{z} = \hat{h}$. The results of panel (a) show that at fixed Re and Pr, the magnitude of the θ profiles decrease with increasing $\hat{\lambda}_T$. It is beneficial to recall that here we have assumed that $\hat{\lambda}$ increases concomitant with $\hat{\lambda}_T$. With increasing $\hat{\lambda}$, the flow is energized and the momentum near the wall increases relative to the classical scenario. In the classical boundary layer, this would lead to a decrease in thermal resistance, corresponding to a thinner boundary layer. Increasing Re leads to a similar decrease in θ, resulting from similar dynamics (thinner boundary layer). Increasing Pr also leads to a decrease in θ because as Pr increases, the ratio of the diffusion rate of momentum normal to the wall to the thermal diffusion rate increases. Thus, the thermal boundary layer

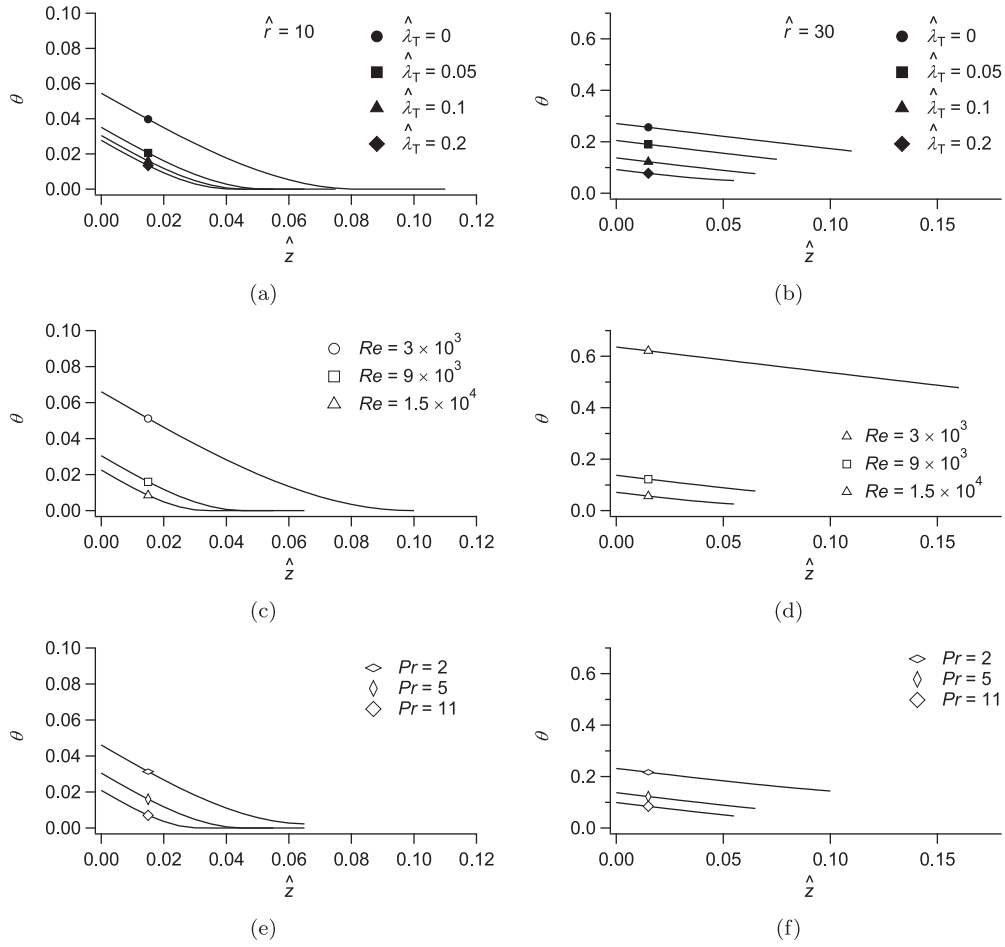

Fig. 4. Non-dimensional temperature profiles as a function of $\hat{z}$. $\hat{r} = 10$ in the left three panels (a, c, and e) and $\hat{r} = 30$ for the right three panels (b, d, and f). In the top two panels (a,b), $Re = 9 \times 10^3$ and $Pr = 5$, with $\hat{\lambda}_T$ varying from 0 to 0.2. In the middle row of panels (c,d), $Pr = 5$ and $\hat{\lambda}_T = 0.1$, with Re varying from 3×10^3 to 1.5×10^4. In the bottom two panels (e,f), $Re = 9 \times 10^3$ and $\hat{\lambda}_T = 0.1$, with Pr varying from 2 to 11.

becomes thinner relative to the hydrodynamic boundary layer, decreasing thermal resistance at the wall. The above behaviors are illustrated in panels a, c, and e of Fig. 4.

Of course, the magnitude of θ increases with $\hat{r}$ as illustrated by comparing the profiles at $\hat{r} = 10$ (left panels) to the profiles at $\hat{r} = 30$ (right panels). The profiles at $\hat{r} = 30$ correspond to region IV of the thin film. Here θ decreases as $\hat{z}$ increases but does not reach zero when $\hat{z} = \hat{h}$ because thermal effects have propagated through the entire film. Now $\theta_{\hat{f}s}$ increases with increasing $\hat{r}$, concomitant with an increasing temperature at the top of the film (due to increased thermal transport moving radially outward). Note that in this region the θ profiles are essentially linear in shape. The variation in the line lengths for each of the profiles shown corresponds to the differences in film thickness for each scenario. At this larger radial location, the spread between the θ profiles for the various $\hat{\lambda}_T$ has increased dramatically. This results because the distance over which $\hat{\lambda}$ and $\hat{\lambda}_T$ have influenced the flow has increased.

Attention is now turned to the local Nusselt number, which is presented as a function of $\hat{r}$ in Figs. 5 and 6. The Nusselt number definition for the isothermal and isoflux cases is identical, where $Nu = q''_w a\pi/(k(T_w(r) - T_j))$ as given earlier in Eq. (21). Fig. 5 includes three panels where Re is varied from 3×10^3 to 1.5×10^4, with Pr held constant at $Pr = 5$. Fig. 6 shows two panels at $Re = 9 \times 10^3$ and with $Pr = 2$ (top) and 11 (bottom). Here we focus on the influence of $\hat{\lambda}_T$ and results are shown in both Figs. 5 and 6 for $\hat{\lambda}_T$ varying from 0 to 0.2. In both figures, Nu results are shown for the isoflux boundary condition corresponding to the current analysis and for the isothermal boundary condition scenario as reported previously [9].

Several important observations may be made concerning the results shown in Figs. 5 and 6. First, Nu decreases as $\hat{r}$ increases. Second, for all $\hat{\lambda}_T$, Nu increases with increasing Re and Pr. These two observations are consistent with classical jet impingement behavior and are not discussed further.

We now turn our attention to the influence of $\hat{\lambda}_T$ and the type of thermal boundary condition (isoflux or isothermal) on the magnitude and variation of Nu. For fixed values of Re and Pr, Nu decreases dramatically as $\hat{\lambda}_T$ increases over the stagnation and initial radial flow region, while a modest increase is observed at larger $\hat{r}$. These results are expected based on the prior study that considered jet impingement on an isothermal superhydrophobic surface [9]. Note that $\hat{r}$ at which the transition from decreasing Nu to increasing Nu occurs depends on Re, Pr, and $\hat{\lambda}_T$. For example, the Re dependence is apparent by comparing panels (a)–(c). We recall that $Pr = 5$ for these results and consider the $\hat{\lambda}_T = 0.1$ case. The radii marking the transition are $\hat{r}$ = 17, 24, and 31 at Re = 3×10^3, 9×10^3, and 1.5×10^4, respectively. The increase in Nu at large $\hat{r}$ is caused by a decrease in the wall temperature relative to the no-temperature jump scenario. This increase in Nu is small but appears in the average isoflux results discussed in Section 3.3.

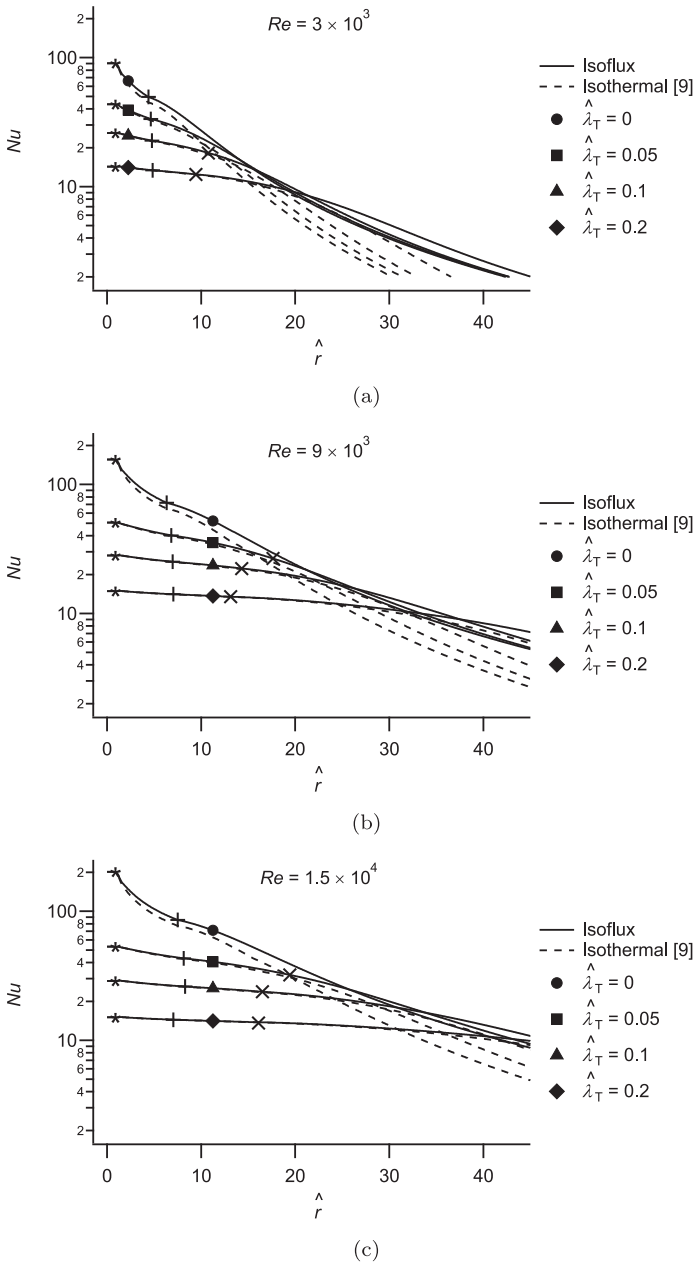

Fig. 5. Local Nusselt number, Nu, as a function of $\hat{r}$ at $Pr = 5$ and $Re = 3 \times 10^3$(top), 9×10^3 (middle), and 1.5×10^4 (bottom). $\hat{\lambda}_T$ varies from 0 to 0.2 in each panel. The region I to II transition, region II to III transition, and region III to IV transition are marked with an asterisk, a plus sign, and a diagonal cross mark, respectively.

For the isoflux case, Nu decreases with increasing $\hat{\lambda}_T$ due to the increased temperature difference (caused by the temperature jump) between the local wall temperature and the temperature of the impinging jet. For the isothermal case, this occurs because the local heat flux decreases (caused by the increased resistance of the air-filled cavities).

The data of Figs. 5 and 6 reveal that the decrease in Nu with increasing $\hat{\lambda}_T$ is greatest at small $\hat{r}$ (in the stagnation zone). To explain this result, consider the expression for the local Nusselt number given by Eq. (25), which has the same form regardless of the thermal boundary condition. When $\hat{\lambda}_T = 0, Nu$ is simply inversely proportional to $\hat{\delta}_T$. In the stagnation zone, $\hat{\delta}_T$ has a relatively small value but then increases as $\hat{r}$ increases, leading to the classical decrease in Nu. When $\hat{\lambda}_T > 0$, the denominator of Eq. (25) is increased by the magnitude of $\hat{\lambda}_T$ and, in the stagnation zone, where $\hat{\delta}_T$ is a small value, this yields an incremental decrease in Nu. Recall that $\hat{\lambda}_T = 0.2$ is approaching the upper limit for realizable normalized temperature jump lengths and, for this value, the Nusselt number in the stagnation zone decreases by more than an order of magnitude.

The functional dependence of Nu on $\hat{\lambda}_T$ and $\hat{\delta}_T$ shown in Eq. (25) explains other important behaviors that are demonstrated in Figs. 5 and 6. As $\hat{\lambda}_T$ increases, the resistance to thermal transport at the wall increases. Thus, depending on the magniude of $\hat{\lambda}_T$, it can exercise much greater influence than $\hat{\delta}_T$ on the magnitude of Nu. Consequently, as $\hat{\lambda}_T$ increases, the Nu profiles show less dependence on $\hat{r}$. This is true for both thermal boundary conditions, where the data level off, showing less dependence on $\hat{r}$. Further, as $\hat{\lambda}_T$ increases, the influence of Re and Pr on the value of Nu also diminish. Recall that

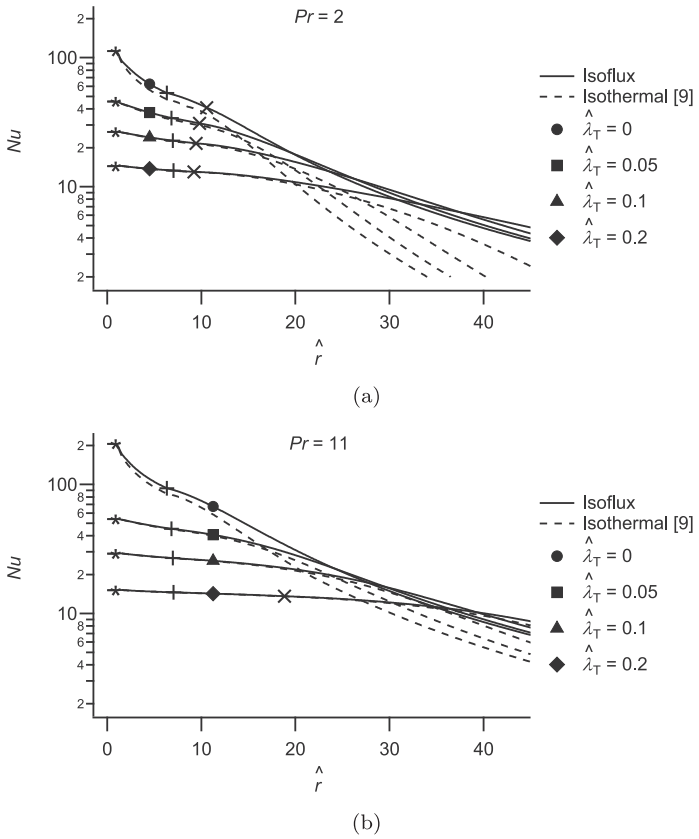

Fig. 6. Local Nusselt number, *Nu*, as a function of $\hat{r}$ at $Re = 9 \times 10^3$ and $Pr = 2$ (top) and $Pr = 11$ (bottom). Results are shown for both the isoflux (current analysis) and isothermal boundary conditions [9] with $\hat{\lambda}_T$ varying from 0 to 0.2. $Pr = 2$ in panel (a) and $Pr = 11$ in panel (b). The region I to II transition, region II to III transition, and region III to IV transition are marked with an asterisk, a plus sign, and a diagonal cross mark, respectively.

variations in *Re* and *Pr* give rise to variations in the thermal boundary layer development and growth. Thus, when $\hat{\lambda}_T$ is large compared to $\hat{\delta}_T$, the influence of *Re* and *Pr* vanishes.

As a final point, we note that isothermal and isoflux results merge together as the temperature jump length increases. The Nusselt number for the isothermal case is always less than the isoflux case, consistent with classical behavior [36]. However, the present results demonstrate that increasing $\hat{\lambda}_T$ decreases and, ultimately eliminates, the influence of the heating condition (isoflux or isothermal) for similar reasoning as described above. When $\hat{\lambda}_T = 0$, *Nu* for the two conditions are equal in the stagnation zone, but begin deviating immediately as $\hat{r}$ increases. When $\hat{\lambda}_T > 0$, the radial location where the two values of *Nu* deviate moves outward. At $Re = 1.5 \times 10^4$, the two *Nu* profiles deviate from each other at $\hat{r} \approx 1$, 12, 25, and 36 for the $\hat{\lambda}_T$ = 0, 0.05, 0.1, and 0.2 scenarios, respectively. This point of departure depends on both *Re* and *Pr*, since these parameters dictate the growth of $\hat{\delta}_T$.

Further insight into this behavior is obtained when considering the relative (percentage) difference between the isoflux and isothermal Nusselt numbers. This is expressed as $1 - Nu_T/Nu_F$, where Nu_T is the local isothermal Nusselt number and Nu_F is the local isoflux Nusselt number. Fig. 7 presents the results of Fig. 5 using this relative difference.

Of course, the relative difference between the isoflux and isothermal Nusselt number is zero within the stagnation region, since the thermal transport here is identical [1]. Upon entering the radial flow region, the relative difference increases with increasing radius. This occurs because of the two terms in the denominator of Eq. (25). Moving outward with $\hat{r}$ results in an increased boundary layer thickness and, since the layers grow at different rates for the two thermal boundary conditions, the relative difference in *Nu* increases. The temperature jump length exercises the same influence on *Nu* for both thermal boundary conditions. Thus, as $\hat{\lambda}_T$ is increased, the relative difference in *Nu* values increases more slowly with increasing $\hat{r}$. The results of Fig. 7 allow estimation of the radial extent over which the local *Nu* values are the same for a range of parameters. Increasing *Re* yields a decrease in the relative difference as well. In general, as *Re* increases, the size of the boundary layer thickness decreases as well and so in Eq. (25), the $\hat{\delta}_T$ term exercises less influence. Although not shown here, variations in *Pr* yield similar behavior.

3.3. Average results

In this section, we consider the radially averaged Nusselt number. Following standard approaches [1], for isothermal scenarios, the average Nusselt number is obtained as

$$\overline{Nu} = \frac{\int_A Nu(T_w - T_j)\,dA}{\int_A (T_w - T_j)\,dA} = \frac{\int_A Nu\,dA}{\int_A dA} \tag{38}$$

and, for isoflux scenarios, the average Nusselt number is obtained as

$$\overline{Nu} = \frac{\int_A q''_w\,dA}{\int_A \frac{q''_w}{Nu}\,dA} = \frac{\int_A dA}{\int_A \frac{1}{Nu}\,dA} \tag{39}$$

Fig. 8 presents the average Nusselt number for the classical no-slip and no-temperature jump scenario so that comparisons may be made with the slip and temperature jump solutions. $\overline{Nu}$ is shown for both thermal boundary conditions as a function of $\hat{r}$ for scenarios where $\hat{\lambda}$ and $\hat{\lambda}_T$ equal zero and the Nusselt number

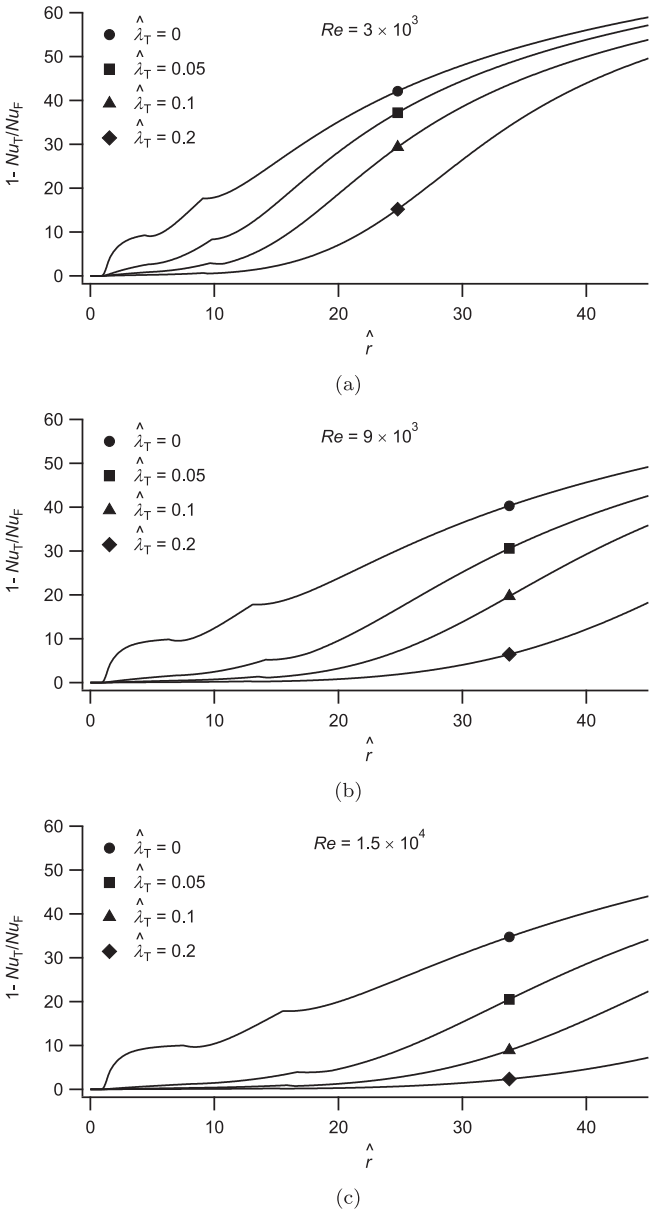

Fig. 7. The relative (percent) difference between the isoflux, Nu_F, and isothermal, Nu_T, local Nusselt numbers relative to the isoflux case is plotted as a function of $\hat{r}$. $Pr = 5$ and Re varies from 3×10^3 to 1.5×10^4. $\hat{\lambda}_T$ varies from 0 to 0.2 in each panel.

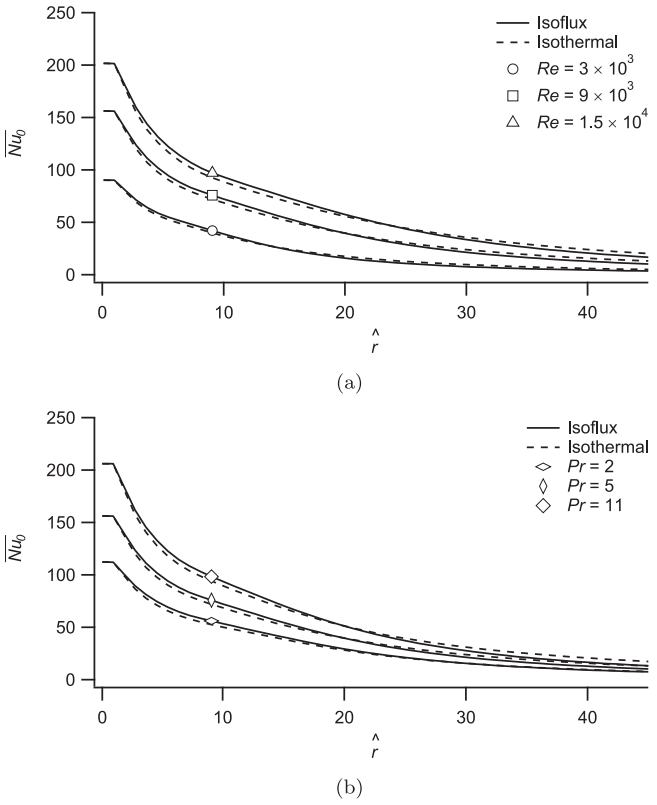

Fig. 8. Average Nusselt number (for no-slip and no temperature jump scenarios), $\overline{Nu}_0$, as a function of $\hat{r}$. Isoflux (solid line) and isothermal (dashed line) results are shown for comparison. Panel (a) displays solutions at $Pr = 5$ with Re varying between 3×10^3 and 1.5×10^4. Panel (b) displays solutions at $Re = 9 \times 10^3$ with Pr varying between 2 and 11.

for this scenario is written with the subscript "0" ($\overline{Nu}_0$). In panel (a), $Pr = 5$ and Re varies from 3×10^3 to 1.5×10^4 and, in panel (b), $Re = 9 \times 10^3$ and Pr varies from 2 to 11.

As has been well established previously, $\overline{Nu}_0$ increases with Re and with Pr because increasing either of these parameters decreases the thickness of the thermal boundary layer. Also, isothermal $\overline{Nu}_0$ is lower than isoflux $\overline{Nu}_0$ for small $\hat{r}$ but becomes greater at large $\hat{r}$. This is a result of averaging the local Nusselt number using the standard approach, where the local Nusselt number is weighted by the temperature difference between the wall and the jet, $T_w - T_j$, and radius (due to the circular area), as shown in Eqs. (38) and (39). For the isothermal case, $T_w - T_j$ is constant so Nu is equally weighted due to temperature difference as $\hat{r}$ varies. For the isoflux case, $T_w - T_j$ increases with $\hat{r}$ and, consequently, Nu at large $\hat{r}$ receives more weighting and, since these Nu are smaller, $\overline{Nu}_0$ decreases. We display these classical results for completeness and to provide a basis of comparison for the slip and temperature jump scenarios below.

The relative decrease (percentage basis) in $\overline{Nu}$ is shown in Fig. 9 for $\hat{\lambda}_T$ varying from 0 to 0.2. $Pr = 5$ and Re varies from 3×10^3 to 1.5×10^4 for both thermal boundary conditions. In each panel, the relative decrease is shown as a function of $\hat{r}$ at $\hat{\lambda}_T = 0.1$ and $\hat{\lambda}_T = 0.2$.

For all scenarios, the relative decrease in $\overline{Nu}$ becomes smaller with increasing radius. This occurs because the influence of the temperature jump length is greatest near the impingement point and, as the averaging radius increases, the area over which temperature jump length plays a negligible role increases. Thus, the impact of the temperature jump yielding a decreased Nu near the impingement point is rapidly overcome. Additionally, as expected, the percentage decrease in $\overline{Nu}$ is greater at higher $\hat{\lambda}_T$ because there is more thermal resistance at the wall, leading to either a decrease in heat flux for the isothermal case or an increase in wall temperature for the isoflux scenario.

At small $\hat{r}$, the percentage decrease for the isothermal and isoflux scenarios are nearly identical. The radial location where the behavior starts to deviate is a function of Re, with increasing Re yielding a larger radial position where the results for the two boundary conditions deviate. An unexpected observation is made at large $\hat{r}$. Here, the percentage decrease remains positive while approaching zero as $\hat{r}$ increases for the isothermal scenario. In contrast, for the isoflux scenario, the percentage decrease in $\overline{Nu}$ becomes negative under certain conditions. This is more pronounced at smaller Re and indicates that $\overline{Nu}$ is actually increasing

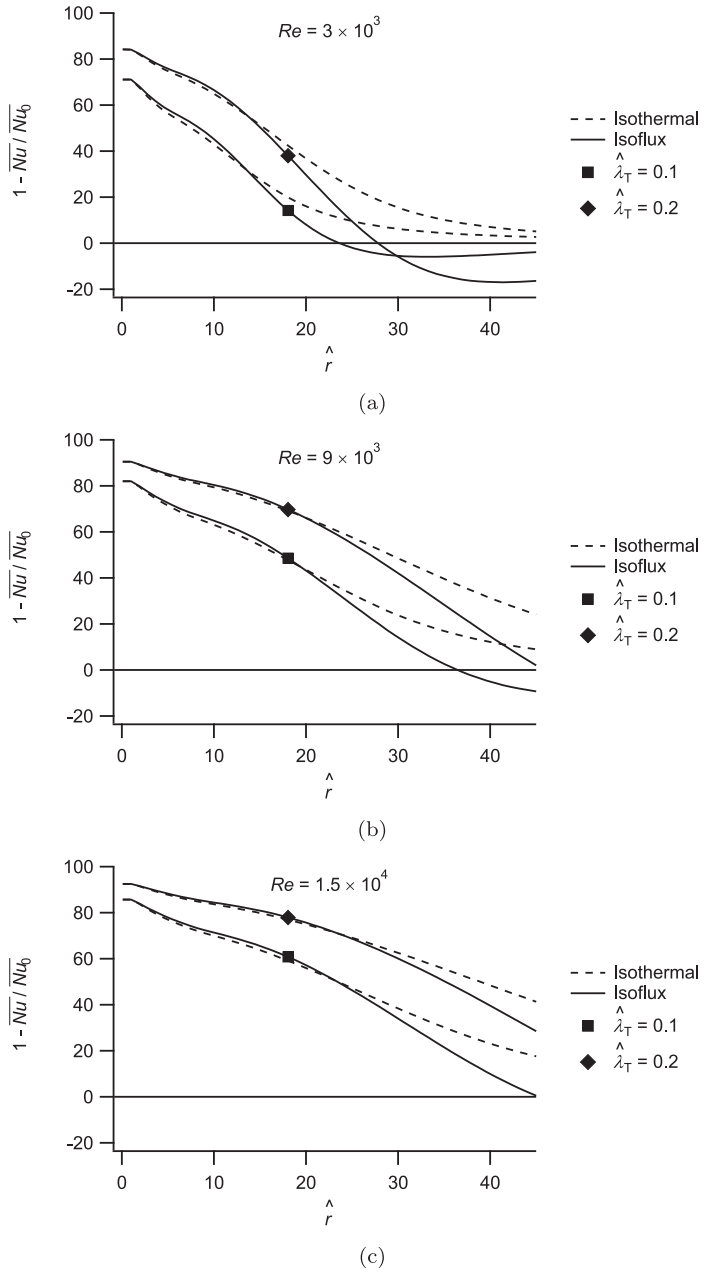

Fig. 9. The relative decrease (percent) in $\overline{Nu}$ as a function of $\hat{r}$. In each panel, the relative decrease is shown for $\hat{\lambda}_T = 0.1$ and $\hat{\lambda}_T = 0.2$ compared to the $\hat{\lambda}_T = 0$ case. $Pr = 5$ for all results and $Re = 3 \times 10^3$, 9×10^3, and 1.5×10^4 in panels (a) through (c).

relative to the no-slip and no temperature jump case at large $\hat{r}$. The $\hat{r}$ location where this occurs is smaller for $\hat{\lambda}_T = 0.1$ than $\hat{\lambda}_T = 0.2$ and decreases as *Re* and *Pr* decrease. As noted earlier, the results with slip and temperature jump for both isoflux and isothermal scenarios become modestly larger than their no-slip and no temperature jump counterparts at large $\hat{r}$. For the isoflux results, this difference receives greater weighting when isoflux *Nu* is averaged than when isothermal *Nu* is averaged. Consequently, the modest increase in *Nu* at large $\hat{r}$ with increasing $\hat{\lambda}_T$ affects $\overline{Nu}$ for the isoflux results and not the isothermal results. We note that the magnitude of $\overline{Nu}$ is small at large $\hat{r}$ and, consequently, the actual increase in $\overline{Nu}$ is also very small.

Fig. 10 presents $\overline{Nu}$ as a function of $\hat{\lambda}_T$. Both isoflux and isothermal results are shown with panel (a) displaying results at $Re = 3 \times 10^3$ and, in panel (b), $Re = 1.5 \times 10^4$. Results are shown where *Nu* is averaged over 10, 20, and 30 radii.

As noted previously, $\overline{Nu}$ decreases as $\hat{\lambda}_T$ increases. For the isoflux case, this occurs because the difference between the average wall temperature and the jet temperature increases and, for the isothermal case, the average heat flux decreases. At small $\hat{\lambda}_T$, $\bar{N}u$ is most sensitive to changes in averaging distance because the local *Nu* has not yet attained the more uniform profile achieved at larger $\hat{\lambda}_T$. Similar to observations made concerning the average results for the no-slip scenario, $\overline{Nu}$ decreases as the averaging radius increases since the area with smaller *Nu* exercises greater influence. As *Re* increases *Nu* increases for all cases because the thermal boundary layer thickness becomes thinner. However, as illustrated in panel (b), at large $\hat{\lambda}_T$, the results become independent of the

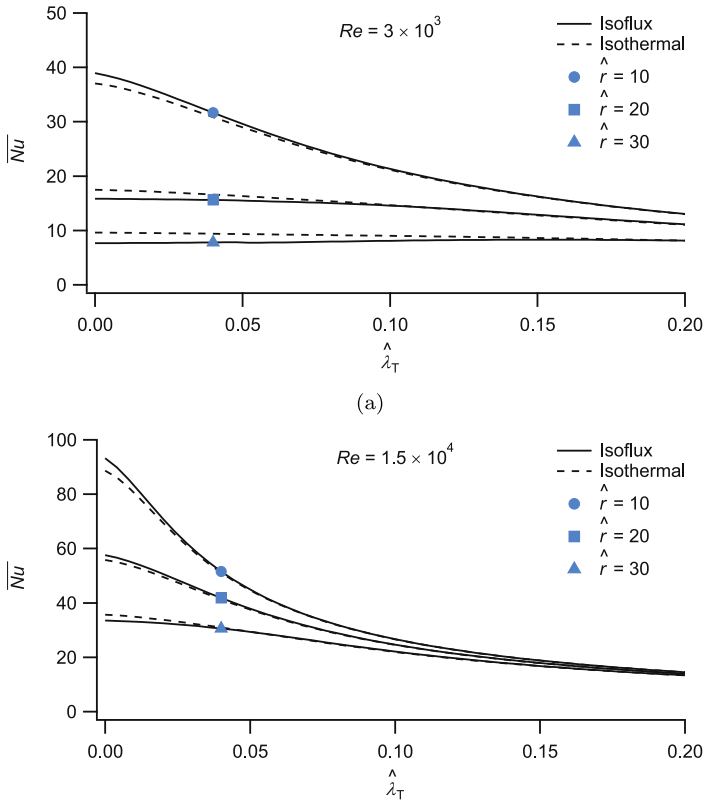

Fig. 10. $\overline{Nu}$ as a function of $\hat{\lambda}_T$ at $Pr = 5$ for $\hat{r}$ varying from 10 to 30. In panel (a), $Re = 3 \times 10^3$ and, in panel (b), $Re = 1.5 \times 10^4$.

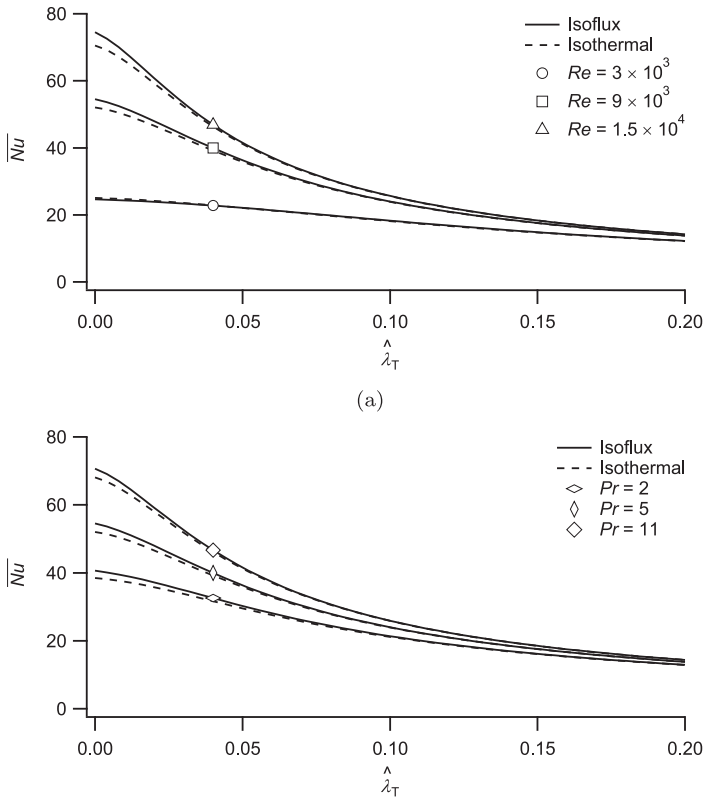

Fig. 11. $\overline{Nu}$ (*Nu* averaged over 15 jet radii) as a function of $\hat{\lambda}_T$. Solutions for both isoflux and isothermal results are shown. Panel (a) presents results at $Pr = 5$ and *Re* varying from 3×10^3 through 1.5×10^4. Panel (b) presents results at $Re = 9 \times 10^3$ for *Pr* varying from 2 through 11.

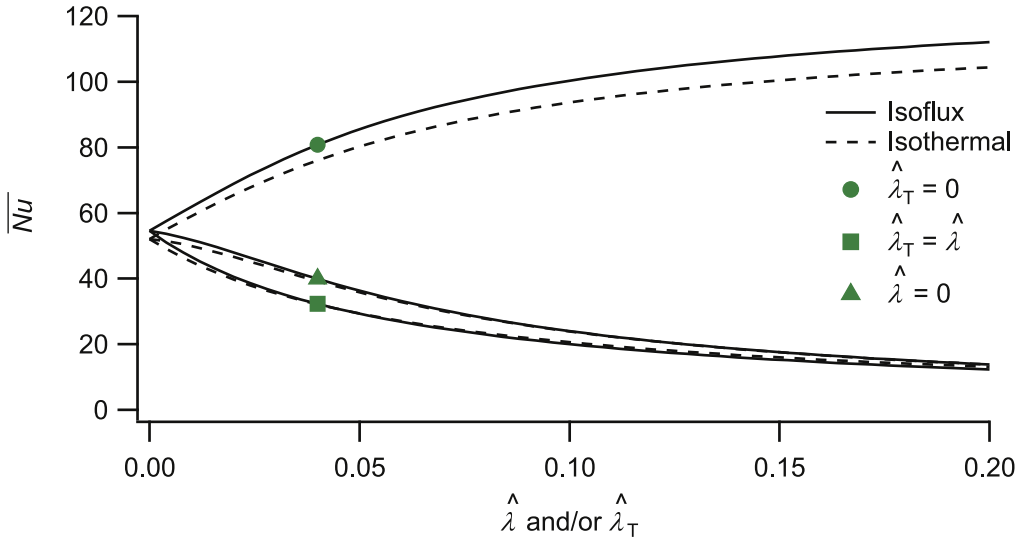

Fig. 12. $\overline{Nu}$ as a function of $\hat{\lambda}$ and/or $\hat{\lambda}_T$. Three scenarios are considered $\hat{\lambda} = 0$ and $\hat{\lambda}_T \neq 0, \hat{\lambda}_T = 0$ and $\hat{\lambda} \neq 0$, and $\hat{\lambda}_T = \hat{\lambda}$. $Pr = 5$ and $Re = 9 \times 10^3$ for all cases.

averaging distance due to the uniform behavior of Nu at large $\hat{\lambda}_T$. Lastly, the difference in $\overline{Nu}$ between the isoflux and isothermal results decreases as $\hat{\lambda}_T$ increases. This trend is expected since the local Nusselt number curves merge together with increasing $\hat{\lambda}_T$.

For completeness, Fig. 11 displays $\overline{Nu}$ (averaged over 15 jet radii) as a function of $\hat{\lambda}_T$ for both the isoflux and isothermal conditions. Panel (a) displays results at $Pr = 5$ and $Re = 3 \times 10^3, 9 \times 10^3$, and 1.5×10^4. Panel (b) displays results at $Re = 9 \times 10^3$ and $Pr = 2$, 5, and 11. The physical reasoning that has already been given will not be repeated. These results are an additional compelling illustration that the influence of heating condition (isoflux or isothermal) and flow properties (Re and Pr) disappear as $\hat{\lambda}_T$ increases.

3.4. Relative importance of slip length and temperature jump length on the solution

On realizable SHPo surfaces, $\hat{\lambda}$ and $\hat{\lambda}_T$ exist as some ratio of each other (typically on the order of 1), depending mainly on the surface microstructure and weakly on the flow conditions [33]. It is beneficial to consider two hypothetical bounding scenarios: one where $\hat{\lambda}_T = 0$ and $\hat{\lambda} \neq 0$ and the other where $\hat{\lambda} = 0$ and $\hat{\lambda}_T \neq 0$. Results corresponding to these two conditions provide theoretical limits for $\overline{Nu}$ at a SHPo surface. A single scenario at $Pr = 5$ and $Re = 9 \times 10^3$ is shown in Fig. 12, where $\overline{Nu}$ (averaged over 15 jet radii) is presented as a function of $\hat{\lambda}$ and/or $\hat{\lambda}_T$. Three cases are shown: $\hat{\lambda}_T = 0$ and $\hat{\lambda} \neq 0, \hat{\lambda} = 0$ and $\hat{\lambda}_T \neq 0$, and $\hat{\lambda} = \hat{\lambda}_T$. When $\hat{\lambda}_T$ and $\hat{\lambda}$ are equal and vary together, the curve tends towards the no-slip ($\hat{\lambda} = 0, \hat{\lambda}_T \neq 0$) result where only $\hat{\lambda}_T$ varies. This indicates that the influence of increased thermal resistance resulting from the larger $\hat{\lambda}_T$ is much greater than the enhanced advection due to the slip boundary condition.

In contrast, when $\hat{\lambda}_T = 0$, much greater $\overline{Nu}$ is achievable due to the slip boundary condition enhancing advection in the absence of temperature jump. Here, the isoflux surface has a larger $\overline{Nu}$ than the isothermal surface (nominally 7% relative to the isothermal surface). However, the $\hat{\lambda}_T = 0$ situation is not physically realizable since all non-wetted SHPo surfaces will exhibit a temperature jump due to the presence of air-filled cavities. Thus, this result is provided solely for illustration.

4. Conclusions

An integral analysis of a liquid jet impinging at an isoflux superhydrophobic surface has been performed. This analysis demonstrates that the introduction of isotropic slip length and temperature jump length to a surface with an isoflux heating condition has similar impact on the thermal transport as the introduction of the same conditions to a surface with an isothermal heating condition.

- The local and average Nusselt numbers are dramatically reduced.
- Local Nusselt number profiles level out, decreasing most significantly with increasing temperature jump length at small radii.
- Flow conditions (Reynolds and Prandtl numbers) exert smaller influence on thermal transport.

We emphasize this work's novel observation that the thermal resistance added by increasing the temperature jump length quickly overcomes the influence of the wall heating condition (isoflux or isothermal) on the Nusselt number such that this dependence on heating condition vanishes at large $\hat{\lambda}_T$.

Declaration of Competing Interest

None declared.

Acknowledgments

Funding: This work was supported by the National Science Foundation [Grant No. CBET-1235881].

References

[1] B.W. Webb, C.-F. Ma, Single-phase liquid jet impingement heat transfer, Adv. Heat Transfer 26 (1995) 105–217, https://doi.org/10.1016/S0065-2717(08)70296-X.
[2] X. Liu, J.H. Lienhard, Liquid jet impingement heat transfer on a uniform flux surface, in: R.K. Shah (Ed.), Heat Transfer Phenomena in Radiation, Combustion, and Fires, vol. 106, ASME HTD, 1989, pp. 523–530.
[3] X. Liu, J.H. Lienhard, J.S. Lombara, Convective heat transfer by impingement of circular liquid jets, J. Heat Transfer 113 (3) (1991) 571–582, https://doi.org/10.1115/1.2910604.

[4] X. Liu, L.A. Gabour, J.H. Lienhard, Stagnation-point heat transfer during impingement of laminar liquid jets: Analysis including surface tension, J. Heat Transfer 115 (1993) 99–105, https://doi.org/10.1115/1.2910677.
[5] C.F. Ma, Y.H. Zhao, Analytical study on impingement heat transfer with single-phase free-surface circular liquid jets, J. Therm. Sci. 5 (4) (1996) 271–277, https://doi.org/10.1007/BF02653234.
[6] J.F. Prince, D. Maynes, J. Crockett, Analysis of laminar jet impingement and hydraulic jump on a horizontal surface with slip, Phys. Fluids 24 (9) (2012) 102103, https://doi.org/10.1063/1.4757659.
[7] J.F. Prince, D. Maynes, J. Crockett, Jet impingement and the hydraulic jump on horizontal surfaces with anisotropic slip, Phys. Fluids 26 (4) (2014) 042104, https://doi.org/10.1063/1.4870650.
[8] J.F. Prince, D. Maynes, J. Crockett, On jet impingement and thin film breakup on a horizontal superhydrophobic surface, Phys. Fluids 27 (2015) 112108, https://doi.org/10.1063/1.4935498.
[9] M. Searle, D. Maynes, J. Crockett, Thermal transport due to liquid jet impingement on superhydrophobic surfaces with isotropic slip, Int. J. Heat Mass Transf. 110 (2017) 680–691, https://doi.org/10.1016/j.ijheatmasstransfer.2017.03.044.
[10] J. Ou, J.P. Rothstein, Direct velocity measurements of the flow past drag-reducing ultrahydrophobic surfaces, Phys. Fluids 17 (10) (2005) 103606, https://doi.org/10.1063/1.2109867.
[11] D. Maynes, K. Jeffs, B. Woolford, B.W. Webb, Laminar flow in a microchannel with hydrophobic surface patterned microribs oriented parallel to the flow direction, Phys. Fluids 19 (9) (2007) 093603, https://doi.org/10.1063/1.2772880.
[12] B. Woolford, J. Prince, D. Maynes, B.W. Webb, Particle image velocimetry characterization of turbulent channel flow with rib patterned superhydrophobic walls, Phys. Fluids 21 (8) (2009) 085106, https://doi.org/10.1063/1.3213607.
[13] J.P. Rothstein, Slip on superhydrophobic surfaces, Annu. Rev. Fluid Mech. 42 (2010) 89–109, https://doi.org/10.1146/annurev-fluid-121108-145558.
[14] R. Fürstner, W. Barthlott, C. Neinhuis, P. Walzel, Wetting and self-cleaning properties of artificial superhydrophobic surfaces, Langmuir 21 (3) (2005) 956–961, https://doi.org/10.1021/la0401011.
[15] B. Bushan, Y.C. Jung, K. Koch, Self-cleaning efficiency of artificial superhydrophobic surfaces, Langmuir 25 (5) (2009) 3240–3248, https://doi.org/10.1021/la803860d.
[16] K. Liu, I. Jiang, Bio-inspired self-cleaning surfaces, Annu. Rev. Mater. Res. 42 (1) (2012) 231–263, https://doi.org/10.1146/annurev-matsci-070511-155046.
[17] D. Miller, J. Crockett, F. Lane, D. Maynes, B. Iverson, Self-cleaning properties via condensation on superhydrophobic surfaces, in: Proceedings of the 2nd Thermal and Fluid Engineering Conference, TFEC2017, American Society of Thermal and Fluids Engineers, Las Vegas, Nevada, 2017.
[18] M. Ma, R.M. Hill, Superhydrophobic surfaces, Current Opin. Colloid Interface Sci. 11 (4) (2006) 193–202, https://doi.org/10.1016/j.cocis.2006.06.002.
[19] E. Lauga, H. Stone, Effective slip in pressure-driven Stokes flow, J. Fluid Mech. 489 (2003) 55–77, https://doi.org/10.1017/S0022112003004695.
[20] Z. Duan, Y.S. Muzychka, Slip flow in the hydrodynamic entrance region of circular and noncircular microchannels, J. Fluids Eng. 132 (2010) 011201, https://doi.org/10.1115/1.4000692.
[21] Z. Kountouriotis, M. Philippou, G.C. Georgiou, Development lengths in Newtonian Poiseuille flows with wall slip, Appl. Math. Comput. 291 (2016) 98–114, https://doi.org/10.1016/j.amc.2016.06.041.
[22] C.E. Clavijo, J. Crockett, D. Maynes, Wenzel to Cassie transition during droplet impingement on a superhydrophobic surface, Phys. Rev. Fluids 1 (2016) 073902, https://doi.org/10.1103/PhysRevFluids. 1.073902.
[23] A. Tuteja, W. Choi, M. Ma, J.M. Mabry, S.A. Mazzella, G.C. Rutledge, G.H. McKinley, R.E. Cohen, Designing superoleophobic surfaces, Science 318 (5856) (2007) 1618–1622, https://doi.org/10.1126/science.1148326.
[24] D. Maynes, B.W. Webb, J. Davies, Thermal transport in a microchannel exhibiting ultrahydrophobic microribs maintained at constant temperature, J. Heat Transfer 130 (2008) 022402, https://doi.org/10.1115/1.2789715.
[25] R. Enright, M. Hodes, T. Salamon, Y. Muzychka, Isoflux Nusselt number and slip length formulae for superhydrophobic microchannels, J. Heat Transfer 136 (2014) 012402, https://doi.org/10.1115/1.4024837.
[26] D. Maynes, J. Crockett, Apparent temperature jump and thermal transport in channels with streamwise rib and cavity featured superhydrophobic walls at constant heat flux, J. Heat Transfer 136 (1) (2014) 011701, https://doi.org/10.1115/1.4025045.
[27] C.-O. Ng, C.Y. Wang, Temperature jump coefficient for superhydrophobic surfaces, J. Heat Transfer 136 (6) (2014) 064501, https://doi.org/10.1115/1.4026499.
[28] C.Y. Wang, Stagnation flows with slip: Exact solutions of the Navier-Stokes equations, Zeitschrift für Mathematik und Physik 54 (1) (2003) 184–189, https://doi.org/10.1007/PL00012632.
[29] C.Y. Wang, Stagnation slip flow and heat transfer on a moving plate, Chem. Eng. Sci. 61 (23) (2006) 7668–7672, https://doi.org/10.1016/j.ces.2006.09.003.
[30] C.Y. Wang, Stagnation flow on a plate with anisotropic slip, Eur. J. Mech. B/Fluids 38 (2013) 73–77, https://doi.org/10.1016/j.euromechflu.2012.10.005.
[31] C. Lee, C.-J. Kim, Maximizing the giant liquid slip on superhydrophobic microstructures by nanostructuring their sidewalls, Langmuir 25 (21) (2009) 12812–12818, https://doi.org/10.1021/la901824d.
[32] C. Ybert, C. Barentin, C. Cottin-Bizonne, P. Joseph, L. Bocquet, Achieving large slip with superhydrophobic surfaces: Scaling laws for generic geometries, Phys. Fluids 19 (2007) 123601, https://doi.org/10.1063/1.2815730.
[33] A. Cowley, D. Maynes, J. Crockett, Effective temperature jump length and influence of axial conduction for thermal transport in superhydrophobic channels, Int. J. Heat Mass Transf. 79 (2014) 573–583, https://doi.org/10.1016/j.ijheatmasstransfer.2014.08.033.
[34] A. Cowley, D. Maynes, J. Crockett, Inertial effect on thermal transport in superhydrophobic microchannels, Int. J. Heat Mass Transf. 101 (2016) 121–132, https://doi.org/10.1016/j.ijheatmasstransfer.2016.05.037.
[35] M. Hodes, L.S. Lam, A. Cowley, R. Enright, S. Maclachlan, Effect of evaporation and condensation at menisci on apparent thermal slip, J. Heat Transfer 137 (7) (2015) 071502, https://doi.org/10.1115/1.4029818.
[36] W. Kays, M. Crawford, B. Weigand, Convective Heat and Mass Transfer, 4th ed., McGraw-Hill Companies, Incorporated, 2005.